Chinese Chemical Letters 37 (2026) 112375

Contents lists available at ScienceDirect

Chinese Chemical Letters

journal homepage: www.elsevier.com/locate/cclet

# Ultrafast synthesis of vacancy-rich $IrO_2/TiO_2$ for acidic oxygen evolution reaction

Lingchang Kong[a], Xiaoya Cui[a,*], Yujing Li[b,*], Kaiwen Yang[c], Hengxing Peng[a], Libing Liao[a], Guocheng Lv[a,*]

[a] Engineering Research Center of Ministry of Education for Geological Carbon Storage and Low Carbon Utilization of Resources, Beijing Key Laboratory of Materials Utilization of Nonmetallic Minerals and Solid Wastes, National Laboratory of Mineral Materials, Hebei Key Laboratory of Resource Low-carbon Utilization and New Materials, School of Materials Science and Technology, China University of Geosciences (Beijing), Beijing 100083, China
[b] School of Materials Science and Engineering, Beijing Institute of Technology, Beijing 100081, China
[c] Institute of Molecular Plus, Department of Chemistry, Tianjin University, Tianjin 300072, China

ARTICLE INFO

*Article history:*
Received 19 December 2025
Revised 6 January 2026
Accepted 8 January 2026
Available online 8 January 2026

*Keywords:*
Proton exchange membrane water electrolysis (PEMWE)
High-temperature shock (HTS)
Supported iridium-based catalyst
Oxygen vacancy ($O_v$)
Adsorbate evolution mechanism (AEM)

ABSTRACT

Supported catalysts are an effective approach in proton exchange membrane water electrolysis (PEMWE) owing to their enhanced metal-support interfacial interaction. We propose a novel high-temperature shock (HTS) technique by Joule-heating to construct an electronic coupling interface between $IrO_2$ nanoclusters catalysts and $TiO_2$ support ($IrO_2/TiO_2$-HTS). The HTS strategy features an ultrafast heating rate and compresses the synthesis time from hours to seconds (2 h to 60 s). The as-prepared catalyst features uniformly embedding the ultrafine $IrO_2$ nanoclusters enrich oxygen vacancies within the redox-active metal oxide matrix, yielding exceptional mass activity and ultrastable performance. The mass activity of the catalyst is 1081 $A/g_{Ir}$ at 1.6 V *vs.* RHE, 13 times higher than of commercial $IrO_2$, and it demonstrates operation time for over 1100 h at 10 $mA/cm^2$ with a voltage decay rate of only 40 μV/h. This HTS strategy offers a scalable route to accelerate vacancy engineering and strong metal oxide-support interaction (SMOSI) formation, enabling high activity at reduced Ir loading and long-term stability under acidic conditions. The approach is general and can be extended to other supported binary oxides, opening opportunities for the development of additional high–performance OER catalysts and PEM–relevant electrolysis systems.

© 2026 Published by Elsevier B.V. on behalf of Chinese Chemical Society and Institute of Materia Medica, Chinese Academy of Medical Sciences.

Proton exchange membrane water electrolysis (PEMWE) has been considered as a promising technology for the production of green hydrogen in a decarbonized future owing to its high current density, hydrogen purity, and conversion efficiency [1–4]. However, its widespread application is hindered by the reliance on rutile-type $IrO_2$, which typically requires iridium (Ir) loadings usually as high as 2-4 $mg_{Ir}/cm^2$ [5,6]. The scarcity-induced high cost of iridium creates a significant barrier to large-scale application [7]. This challenge is clearly outlined by the U.S. Department of Energy (DOE) 2026 technical targets, which call for a substantial reduction in noble metal loading to 0.5 $mg/cm^2$ while achieving 3.0 $A/cm^2$ @ 1.8 V in PEMWE [8]. This highlights the urgent need to enhance the intrinsic catalytic activity of iridium. To address this challenge, developing supported catalysts [9,10] has become an effective strategy to improve iridium utilization by exposing more catalytic sites and providing robust anchoring of nanoparticles. Representative catalysts such as $IrO_2$@$TiO_2$ [11], Ir/$CeO_x$ [12], and $IrO_2$@$TaO_x$@TaB [13] show enhanced catalytic performance. Support materials such as $TiO_2$ [14], $SnO_2$ [15–17], $TaO_x$ [18,19], $MnO_2$ [20], $Co_3O_4$ [21], and $NbO_x$ [22–24] can suppress catalyst agglomeration and dissolution, thereby mitigating the loss of active sites.

In recent years, the synthesis of supported iridium-based catalysts has been extensively investigated, including high-temperature annealing [18,25–27], photo/electrodeposition [28,29], co-precipitation [14,20], and wet-chemical reduction [12,30]. Yu *et al.* [31] employed wet-chemical reduction to synthesize an amorphous $IrO_x$ layer on a hollow $TiO_2$ porous structure. However, post-annealing at 150 °C for 1 h was still required to achieve long-term stability (600 h@10 $mA/cm^2$). Wang *et al.* [26] developed low Ir-loading catalysts *via* the Adams fusion method, which exhibited stable operation for over 500 h at 500 $mA/cm^2$ in a PEM electrolyzer. Nevertheless, the synthesis involved a 3 h heating process with high energy consumption. Similarly, Wang *et al.* [32] constructed a continuous 15 nm $IrO_x$ coating layer through one-step

* Corresponding authors.
*E-mail addresses:* xiaoyacui@cugb.edu.cn (X. Cui), yjli@bit.edu.cn (Y. Li), guochenglv@cugb.edu.cn (G. Lv).

https://doi.org/10.1016/j.cclet.2026.112375
1001-8417/© 2026 Published by Elsevier B.V. on behalf of Chinese Chemical Society and Institute of Materia Medica, Chinese Academy of Medical Sciences.

annealing, achieving both a p-n junction interface and a conductive network. However, this approach suffered from high energy consumption and prolonged processing time. Zhang *et al.* [12] employed the polyol reduction method to synthesize an $Ir/CeO_x$ catalyst demonstrating outstanding durability with a voltage decay of 1.33 μV/h over 6000 h. Nonetheless, this strategy required ultrasonic assistance and prolonged aging time (3 h). Overall, the synthesis of these advanced supported catalysts reveals their own set of difficulties. Conventional approaches typically require protracted processing times, high energy consumption, and complex steps that can leave residues or cause undesirable particle agglomeration. Consequently, developing an ultrafast synthesis protocol that enables uniform anchoring of active sites and strong interfacial interactions is highly desirable.

The Joule heating-triggered high-temperature shock (HTS) strategy reported by Chen *et al.* [33–35] is characterized by an ultrarapid heating/cooling rate ($>10^5$ K/s). This technique not only shortens synthesis times from hours to seconds but also reduces energy consumption [36]. Moreover, the rapid, non-equilibrium reaction kinetics can stabilize ultrafine nanoparticles and introduce a high density of beneficial defects (*e.g.,* oxygen vacancy and Frank dislocation) [37,38]. Oxygen vacancies, in particular, can tune the electronic configuration of the catalyst and decrease charge-transfer resistance. Such modulation helps reduce the adsorption energy of catalytic intermediate species and lower the energy barrier of the rate-determining step (RDS), leading to substantial improvements in catalytic activity [39,40]. The HTS technique has been extensively employed in the rapid synthesis of binary alloys, high-entropy alloys. and supported electrocatalysts. For instance, Huang *et al.* [41] converted Ir precursors to $IrO_2$ clusters ($IrO_2$@$Co(OH)_2$-NF) *via* a two-step Joule-heating process. The process preserved the layered support matrix and cluster active sites while strengthening electronic coupling between clusters and the support. Gao *et al.* [42] employed a millisecond HTS technique to synthesize carbon-supported $Ir_3Ni$ alloy nanoparticles with an average size of 4.85 nm, achieving a mass activity of 2.37 $A/mg_{Ir}$. Similarly, Chen *et al.* [43] prepared a dislocation-strained IrNi alloy *via* a non-equilibrium HTS route, where high-energy surfaces induced by dislocations can efficiently inhibit surface reconstruction. Cui *et al.* [44] developed a liquid-HTS synthesis of high-entropy alloys (PtCoNiRuIr) in 60 s with controlled composition and lattice strain. Zhou *et al.* [45] successfully synthesized $Fe_{0.15}Co_{0.40}Ni_{0.05}Pt_{0.32}Pd_{0.08}$ high-entropy alloys *via* rapid pulsed heating avoiding metal segregation and immiscibility in a multi-metal system. The HTS technique enables precise regulation of metal-support interfaces and defect distributions at the nanoscale, underpinning it as an irreplaceable approach for interface engineering. However, the HTS strategy is limited to single-phase construction with no systematic investigation into the correlation between crystal phase and catalytic activity. Additionally, the rapid atomic migration during HTS leads to a failure to directional exposure of high-active facets.

Applying the HTS strategy, we synthesized a high-density $IrO_2$ catalyst supported on a $TiO_2$ matrix ($IrO_2/TiO_2$-HTS) in only 60 s. This approach facilitates the formation of highly dispersed $IrO_2$ nanoclusters with an average size of 1.95 nm, which are enriched with oxygen vacancies. The developed HTS strategy synergistically constructs a stable structure with ultrafine clusters, high defect density, and robust interfaces, all of which collectively contribute to the excellent catalytic performance. The as-prepared catalyst demonstrates outstanding oxygen evolution reaction (OER) activity and acid corrosion resistance. The versatility of the HTS method is further shown by its applicability to other systems, such as Ru-doped $IrO_2/TiO_2$. This work, therefore, provides a new and efficient route for the rational design and ultrafast synthesis of advanced supported catalysts for PEMWE.

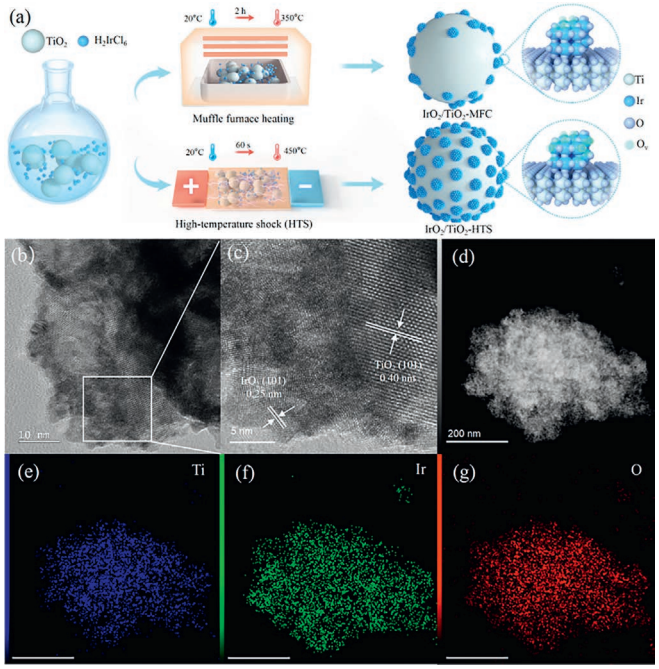



**Fig. 1.** (a) Schematic diagram of $TiO_2$ supported $IrO_2$ nanocluster difference in the muffle furnace and HTS sample. (b, c) Transmission electron microscopy (TEM) image. (d-g) STEM images with corresponding elemental mapping images.

As schematically shown in Fig. 1a, we report a molten-salt-assisted approach for the fabrication of supported $IrO_2$ catalysts ($IrO_2/TiO_2$-HTS) *via* Joule heating-triggered HTS technique in a $NaNO_3$ oxidation environment. In contrast to the reported $TiO_2$-supported $IrO_2$ catalysts (*e.g.,* W-$TiO_2$@$IrO_2$, $IrO_2$@$TiO_2$, and Ir/a.$TiO_2$) [46–48] prepared previously by mechanical agitation and conventional calcination (tube furnace, muffle furnace, *etc.*). We first utilized HTS technique to synthesize $IrO_2/TiO_2$ catalyst for acidic water electrolysis, greatly reducing the preparation time (Table S1 in Supporting information). Detailed experimental procedures are provided in Supporting information. As illustrated in Fig. 1a, the synthesis initiates with electrostatic attraction of a negatively charged iridium precursor onto the positively charged surface of the $TiO_2$ support, facilitating the bottom-up encapsulation of iridium precursor within $TiO_2$ nanoislands (Fig. S1 in Supporting information). A key benefit of the HTS method lies in its rapid and uniform heating, which is visually confirmed by a uniform yellow light across the HTS substrate (Fig. S2 in Supporting information). In contrast, conventional muffle furnace heating depends on slower thermal conduction [49]. The Joule-heating strategy achieves a heating rate of 26 K/s for 450 °C and a subsequent quenching rate of 15 K/s, significantly reducing the synthesis time from 2 h to just 60 s (Figs. S3 and S4 in Supporting information).

The ultrafast processing kinetically suppresses crystal growth and phase separation, which are common issues in prolonged high-temperature fabrication. The rapid duration time enables precise control of the catalyst's microstructure, resulting in the formation of ultrasmall $IrO_2$ particles, abundant oxygen vacancies, and strong interfacial coupling. The HTS approach allows for a higher metal oxide loading with homogeneous distribution compared to equilibrium-driven synthesis. Moreover, the versatility of the HTS strategy was confirmed by its successful application to other systems, including $IrO_2/TiO_2$ nanosheets and Ru-doped $IrO_2/TiO_2$ (Figs. S5-S8 in Supporting information). The supported binary oxides, which showed no signs of metal segregation, proved its broad applicability for designing advanced supported catalysts. Furthermore, the adaptability of this methodology demonstrates its

broad applicability to other support (*e.g.*, TiN, $MnO_2$, $Co_3O_4$, and $SnO_2$) and dopants (*e.g.*, transition metal elements (TEMs) and rare earth elements (REEs)), co/multi-doping, and high-entropy oxides (HEOs) strategies for supported $IrO_2$-based systems. Artificial intelligence (AI)-assisted synthesis can provide precise guidance for high-throughput catalyst design, thereby significantly enhancing catalyst fabrication efficiency.

Physicochemical analyses were performed to analyze the structure and morphology of the synthesized $IrO_2/TiO_2$-HTS catalyst. Transmission electron microscopy (TEM) images displayed that the anatase $TiO_2$ support consists of spheroidal nanoparticles (25.7 nm) with a lattice spacing of 0.358 nm, corresponding to the (101) plane (Fig. S9 in Supporting information) [50]. Nitrogen adsorption-desorption analysis suggested a porous structure with a high specific surface area of 80.88 $m^2/g$ and an average pore size of 21.26 nm (Fig. S10 in Supporting information). Such porosity is beneficial for PEMWE as it facilitates mass transport and bubble detachment from the active sites [51]. Compared with commercial $IrO_2$, the HTS-synthesized $IrO_2$ nanoclusters preferentially expose the (101) crystal facet, whereas commercial $IrO_2$ predominantly exposes the less active (110) facet with an average particle size of 12.8 nm (Figs. S11 and S12 in Supporting information). Previous studies have shown the (101) facet has a lower energy barrier for the oxygen evolution reaction, suggesting superior intrinsic activity [27].

Further TEM analysis confirmed the uniform dispersion of ultrafine $IrO_2$ nanoclusters, with an average particle size of 1.95 nm, across the $TiO_2$ support (Figs. 1b and c, Fig. S13 in Supporting information). High-resolution imaging clearly showed an intimate contact interface between the $IrO_2$ ((101) and (200) facets) and the $TiO_2$ (101) facet (Figs. 1b and c, Fig. S13) [11]. This well-defined interface is critical for promoting efficient electron transport and enhancing catalytic stability. Energy-dispersive X-ray spectroscopy (EDX) mapping confirmed the homogeneous distribution of elements, with mass ratios of 44.06% Ir, 20.75% Ti, and 35.19% O (Figs. 1d-g, Fig. S14 and Table S2 in Supporting information). The higher density of Ir relative to the muffle-furnace sample (36.55% Ir in Figs. S15 and S16 in Supporting information) highlights the superior dispersion capability and strong anchoring effect of the $TiO_2$ support for $IrO_2$. Additionally, inductively coupled plasma optical emission spectroscopy (ICP-OES) results showed elemental contents slightly higher than EDS results, with Ir and Ti mass fractions of 45.27% and 28.24%, respectively (Table S3 in Supporting information). The surface properties were evaluated using water contact angle measurements (Fig. S17 in Supporting information) [52]. Compared with the muffle-furnace route ($CA = 16.6°$), the HTS-derived catalysts displayed a smaller contact angle ($CA = 9.1°$), indicative of a super-hydrophilic surface. A super-hydrophilic surface facilitates intimate contact between the aqueous electrolyte and solid electrode, promoting bubble detachment and avoiding the active sites from being blocked.

To gain deeper insights into the structural evolution of the catalysts, X-ray diffraction (XRD) patterns of anatase $TiO_2$ matrix, commercial $IrO_2$ (Com $IrO_2$), $IrO_2$ prepared by HTS ($IrO_2$-HTS), $IrO_2/TiO_2$-MFC and $IrO_2/TiO_2$-HTS were employed to analyze the crystal structure. For the $TiO_2$ matrix (Fig. S18 in Supporting information), it was found that all the diffraction peaks match well with characteristic peaks of anatase $TiO_2$ (PDF #21-1272), where the diffraction peak in the $2\theta$ range of 25.28° corresponds to the (101) facet of anatase $TiO_2$. The $IrO_2$-HTS sample show similar crystal structures with rutile $IrO_2$ (PDF #43-1019). Two characteristic peaks at 28.0° and 34.7° were attributed to the (110) and (101) planes of $IrO_2$. Additionally, compared with Com $IrO_2$, the characteristic peaks of $IrO_2$-HTS showed a progressive broadening indicating ultrasmall size (Figs. S12 and S19 in Supporting information). Furthermore, the XRD patterns of the $IrO_2/TiO_2$ composites (Fig. 2a) displayed two distinct characteristic peaks that correspond to the (101) and (200) facets of $TiO_2$. A broadened diffraction peak in the $2\theta$ range of 30°-40° was also observed, which corresponds to the (101) facet of $IrO_2$ [53]. In fact, $IrO_2$ signals in the $IrO_2/TiO_2$ composites are hard to distinguish clearly in Fig. 2a. The main reason for this phenomenon is that the small-sized $IrO_2$ nanoclusters induce diffraction peak broadening, together with the preferential exposure of the highly active (101) facet. This finding is consistent with the XRD results mentioned earlier. These observations demonstrate the successful synthesis of $IrO_2/TiO_2$ composites featuring ultrasmall $IrO_2$ nanoclusters.

The electronic structure and defect concentration of the catalysts were investigated to understand the origins of the enhanced catalytic performance. Electron paramagnetic resonance (EPR) spectroscopy exhibited a distinct signal at $g = 2.003$, which is characteristic of oxygen vacancy ($O_v$). The signal intensity was higher for the $IrO_2/TiO_2$-HTS catalyst than for its counterpart prepared by a conventional muffle furnace ($IrO_2/TiO_2$-MFC), suggesting that the HTS process introduces a higher concentration of oxygen vacancies (Fig. 2b and Fig. S20 in Supporting information). This finding was further supported by X-ray photoelectron spectroscopy (XPS), where XPS survey spectrum shows the presence of Ir, Ti, and O signals for $IrO_2/TiO_2$-HTS (Fig. S21 in Supporting information). High-resolution O 1s spectra showed that the relative area of the peak associated with oxygen vacancies (531.45 eV) was significantly larger for $IrO_2/TiO_2$-HTS (54%) than for $IrO_2/TiO_2$-MFC (32%) (Fig. 2c) [54]. The generation of these oxygen vacancies is critical, because they can accelerate charge transfer, improve electrical conductivity, and enhance oxygen evolution reaction (OER) activity [39]. Further XPS analysis provided direct evidence of strong electronic interactions between the catalyst and the support. The Ti 2p peaks for $IrO_2/TiO_2$-HTS shift positively of 0.5 eV relative to pure $TiO_2$ matrix [55], while the Ir 4f peaks shifted negatively by 0.5 eV compared with unsupported $IrO_2$-HTS (Figs. 2d and e) [39,56] The Ir 4f spectra showed the coexistence of $Ir^{4+}$ and $Ir^{3+}$ species in $IrO_2/TiO_2$-HTS, indicating an increase in the oxidation state of titanium and a corresponding reduction in the oxidation state of iridium, consistent with electron transfer from support to the catalyst ($Ti \rightarrow O \rightarrow Ir$). This charge redistribution is a signature of strong metal oxide-support interaction (SMOSI). This conclusion was further supported by Raman spectroscopy (Fig. 2f). In the composite catalyst, the primary $E_{g(1)}$ vibrational mode of $TiO_2$ displayed a blue shift. This shift provides additional evidence of the modified electronic environment at the $IrO_2/TiO_2$ interface, and is consistent with the charge transfer identified by XPS [57,58].

To evaluate the electrocatalytic performance for the acidic OER, the synthesized $IrO_2/TiO_2$-HTS catalyst was tested in a 0.5 mol/L $H_2SO_4$ electrolyte and compared against several control samples. The $Hg/Hg_2SO_4$ reference electrode was calibrated using the hydrogen evolution reaction (HER) method, yielding a potential of 0.652 V *vs.* RHE (Fig. S22 in Supporting Information). As shown in Fig. 3a, linear sweep voltammetry (LSV) curves revealed that $IrO_2/TiO_2$-HTS demonstrates the highest OER activity. It required an overpotential of only 245 mV to achieve a current density of 10 $mA/cm^2$, outperforming $IrO_2/TiO_2$-MFC (250 mV), $IrO_2$-HTS (285 mV) and commercial $IrO_2$ (317 mV). This enhanced activity, which surpasses that of many recently reported Ir-based catalysts (*e.g.,* $SrIr_2O_6$ [59]) and supported Ir-based catalysts (*e.g.*, $IrO_2/TiO_{2-x}$, Ir-Ir$\alpha MnO_2$, and $IrO_2$@$TaO_x$@TaB [19,60,61]) (Fig. 3b and Table S4 in Supporting information), is attributed to the combination of ultrafine $IrO_2$ nanoclusters, a high concentration of oxygen vacancies, and a stable catalyst-support interface. It is widely recognized that the turnover frequency (TOF) serves as a reliable indicator of intrinsic catalytic activity. As shown in Fig. S23 (Supporting information), the TOF values of all the catalysts gradually increase with increasing overpotential. Notably, $IrO_2/TiO_2$-HTS possesses

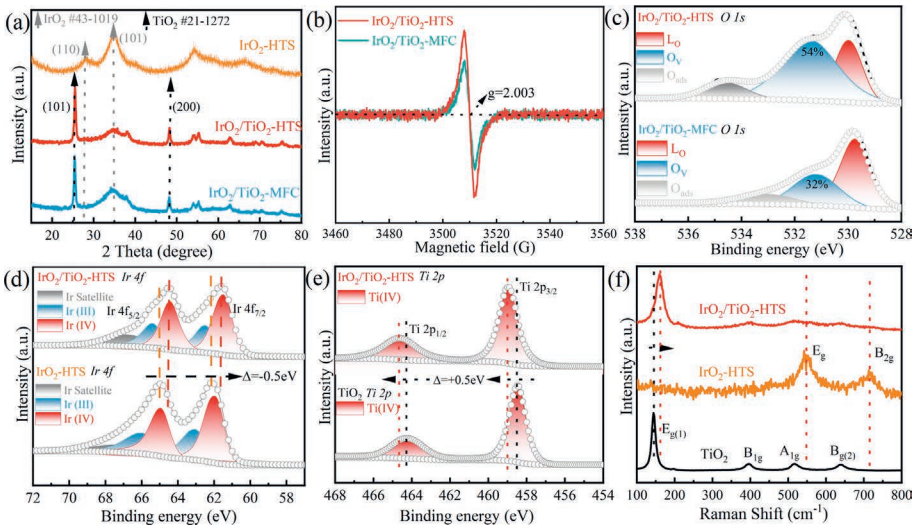



**Fig. 2.** Structural characterization of $IrO_2/TiO_2$-HTS. (a) XRD patterns of $IrO_2/TiO_2$-HTS and $IrO_2/TiO_2$-MFC. (b) EPR spectra of $IrO_2/TiO_2$-HTS and $IrO_2/TiO_2$-MFC. (c) High-resolution XPS O 1s spectra of $IrO_2/TiO_2$-HTS and $IrO_2/TiO_2$-MFC. (d) High-resolution XPS Ti 2p spectra of $IrO_2/TiO_2$-HTS and pure$TiO_2$. (e) High-resolution XPS Ir 4f spectra of $IrO_2/TiO_2$-HTS and $IrO_2$-HTS. (f) Raman spectra of $IrO_2$-HTS, pure $TiO_2$ and $IrO_2/TiO_2$-HTS. $TiO_2$ matrix exhibited four Raman peaks at 143, 396, 516 and 638 $cm^{-1}$, assigned to the $E_{g(1)}$, $B_{1g}$, $A_{1g}$ and $E_{g(2)}$ modes, respectively. These vibrations originate from symmetric stretching, symmetric bending, and asymmetric bending of the anatase $TiO_2$. $IrO_2$-HTS showed two characteristic peaks at 546 and 714 $cm^{-1}$, corresponding to $E_g$ and $B_{2g}$ stretching modes of Ir – O bonds.

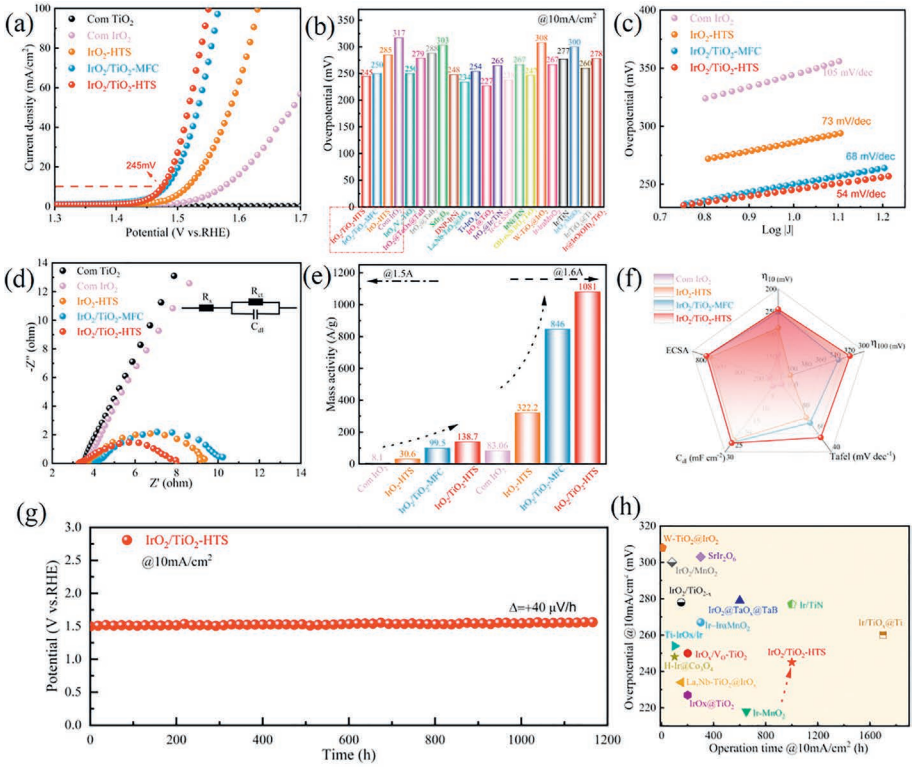



**Fig. 3.** Comparison of acidic OER performance of catalysts in 0.5 mol/L $H_2SO_4$ electrolyte (Commercial $IrO_2$, pure $TiO_2$, $IrO_2$-HTS, $IrO_2/TiO_2$-MFC and $IrO_2/TiO_2$-HTS). (a) LSV curves. (b) Overpotential comparison at 10 $mA/cm^2$ with previously reported Ru-, Ir- and RuIr-based acidic OER catalysts. (c) Tafel plots. (d) Nyquist plots obtained at 1.5 V *vs.* RHE in the frequency range of 0.1-100 kHz, the inset shows the equivalent circuit model. (e) MA of Com $IrO_2$, $IrO_2$-HTS, $IrO_2/TiO_2$-MFC, $IrO_2/TiO_2$-HTS at 1.45 and 1.5 V *vs.* RHE. (f) Radar chart summarizing crucial parameters including $C_{dl}$, Tafel slope, ECSA and overpotential at 10 and 100 $mA/cm^2$. (g) Chronopotentiometric stability tests of $IrO_2$-HTS and $IrO_2/TiO_2$-HTS at 10 $mA/cm^2$. (h) Comparison of activity (overpotential at 10 $mA/cm^2$) and durability (operation time at 10 $mA/cm^2$) with recently reported Ru-, Ir- and RuIr-based catalysts.

the highest TOF values across the whole overpotential, indicating its superior intrinsic activity. The reaction kinetics were further assessed using Tafel analysis, where $IrO_2/TiO_2$-HTS exhibited a slope of 54 mV/dec, significantly lower than that the control sample (Fig. 3c), indicating more favorable reaction kinetics. This is consistent with its higher double-layer capacitance ($C_{dl}$) of 26.3 $mF/cm^2$ and larger electrochemically active surface area (ECSA), which confirm a greater number of exposed active site (Fig. S24 in Supporting information). Furthermore, electrochemical impedance spectroscopy (EIS) showed that $IrO_2/TiO_2$-HTS possessed the lowest charge-transfer resistance ($R_{ct} = 2.5\ \Omega$), confirming its excellent electronic conductivity (Fig. 3d). Consequently, the catalyst

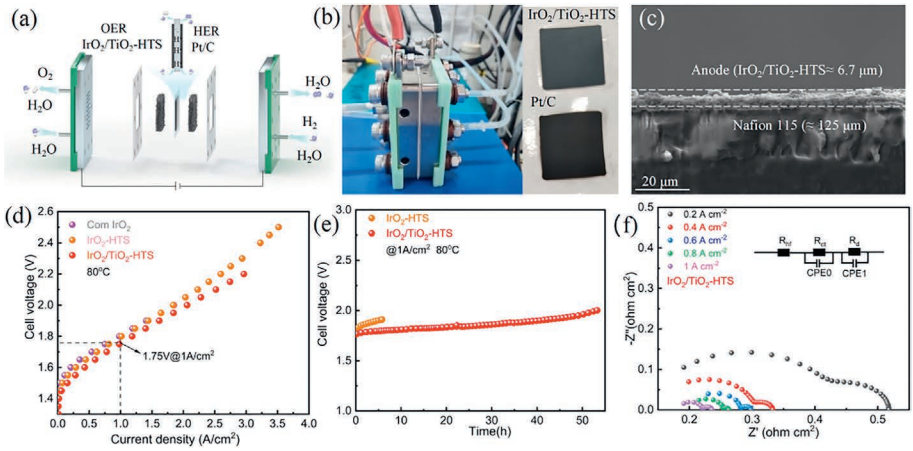



**Fig. 4.** PEMWE performance. (a) Schematic diagram of PEMWE device. (b) Digital photograph of PEMWE setup, showing the anode and cathode catalysts layer coated *via* CCM technique. (c) Cross-sectional SEM image of the MEA. (d) PEMWE performance evaluation form polarization curves. (e) Chronopotentiometric test at 1 A/cm$^2$ in the PEM electrolyzer. (f) EIS test under different current density.

achieved a mass activity of 1081 A/$g_{Ir}$ at 1.6 V *vs.* RHE, a value 13 times higher than that of commercial $IrO_2$ (Fig. 3e). Radar plots comparing overpotential at 10 and 100 mA/cm$^2$, ECSA, $C_{dl}$, and Tafel slopes, further highlight the superior OER kinetics of $IrO_2/TiO_2$-HTS (Fig. 3f).

The durability of the catalysts, a critical parameter for practical applications, was evaluated through long-term chronopotentiometry tests. The $IrO_2/TiO_2$-HTS catalyst demonstrated exceptional stability, operating continuously for 1165 h at a constant current density of 10 mA/cm$^2$ with a voltage decay of only 40 μV/h (Fig. 3g). In stark contrast, the $IrO_2$-HTS and $IrO_2/TiO_2$-MFC catalysts failed after only 363 h and 70 h, respectively (Fig. S25 in Supporting information). Moreover, $IrO_2/TiO_2$-HTS catalyst could maintained stable operation for over 45 h (Fig. S26 in Supporting information). The structural integrity of the $IrO_2/TiO_2$-HTS catalyst was confirmed by minimal iridium leaching (4.4 % after 100 h and 6.4 % after 300 h), and post-mortem XPS analysis, which showed that the Ir oxidation states and oxygen vacancy concentration was preserved (Table S5 and Fig. S27 in supporting information). The strong interaction between $IrO_2$ and the $TiO_2$ support is credited for this enhanced durability. The overall performance profile of the HTS-synthesized catalyst in terms of both activity and stability is superior to many recently reported Ir-based systems (Fig. 3h and Table S6 in Supporting information). The TEM image and corresponding EDX analyses after OER (Fig. S28 in Supporting Information) verified that the $IrO_2$ clusters remained uniformly distributed on the $TiO_2$ surface, and negligible structural or compositional changes were detected, indicating its excellent durability and structural integrity during OER.

To assess its viability in a practical device, the $IrO_2/TiO_2$-HTS catalyst was integrated as the anode in a membrane electrode assembly (MEA) for a full-cell PEMWE test. The schematic configuration of the PEMWE device is shown in Fig. 4a, consisting of a proton exchange membrane N115, catalyst layer (CL), gas diffusion layer (GDL), and bipolar plate (BP). The MEA as the core component in PEMWE is composed of the proton exchange membrane, CL and GDL, and prepared *via* a catalyst-coated membrane (CCM) spraying technique for water electrolysis. As shown in Fig. 4b, both anode and cathode layer were uniformly coated, where anode employed $IrO_2/TiO_2$-HTS with Ir loading of 1 mg$_{Ir}$/cm$^2$ and cathode employed commercial Pt/C with Pt loading of 0.35 mg$_{Pt}$/cm$^2$. The cross-sectional scanning electron microscope (SEM) of MEA presented the anode catalyst layer thickness of 6.7 μm and corresponding elemental mapping confirmed the homogeneous distribution of Ir, Ti and O, indicating a compact and well-integrated catalysts layer (Fig. 4c and Fig. S29 in Supporting information). After optimizing the operating temperature and water flow rate (Figs. S30 and S31 in Supporting information), the performance of the MEA was evaluated. At 80 °C, the MEA incorporating the $IrO_2/TiO_2$-HTS catalyst required a cell voltage of only 1.75 V to achieve a current density of 1 A/cm$^2$, surpassing the performance of MEAs based on $IrO_2$-HTS and commercial $IrO_2$ (Fig. 4d). Furthermore, the device demonstrated stable operation for 50 h at this high current density (Fig. 4e). These results validate the practical potential of the ultrafast HTS synthesis method for producing highly active and durable electrocatalysts for industrial-scale green hydrogen production. The EIS are performed at different current densities and the impedance of MEA decreases as the current density increases (Fig. 4f).

To determine the origin of the enhanced catalytic performance of $IrO_2/TiO_2$-HTS catalyst, a combination of electrochemical and *in situ* analytical techniques was employed. The adsorption behaviors of oxygen intermediates, which is a critical factor in OER activity, was first investigated. The methanol oxidation reaction (MOR) was used as a probe, as the electrophilic *OH intermediate, the first species formed during OER, readily reacts with nucleophilic methanol. A stronger *OH adsorption on the catalyst surface leads to a more pronounced MOR current [62–64]. When methanol was introduced, a significantly larger increase in current density was observed for $IrO_2/TiO_2$-HTS compared to $IrO_2$-HTS confirming stronger *OH adsorption on the supported catalyst (Fig. 5a) [21,65,66]. Furthermore, cyclic voltammetry (CV) revealed two distinct pairs of redox peaks for both catalysts, corresponding to the formation of intermediates *via* water deprotonation (Fig. 5b) The catalytic activity of $IrO_2/TiO_2$-HTS was also found to be independent of pH, a characteristic feature of the adsorbate evolution mechanism (AEM) (Fig. 5c) [67].

To obtain direct experimental evidence of the reaction pathway, *in-situ* spectroscopic and mass spectrometry analyses were performed. *In situ* attenuated total reflection surface-enhanced infrared absorption spectroscopy (ATR-SEIRAS) (Fig. 5d and Fig. S32 in Supporting information) was used to monitor surface species under different potential. For both $IrO_2/TiO_2$-HTS and $IrO_2$-HTS, vibrational bands corresponding to of *OH (3200 cm$^{-1}$) and *OOH (880 and 1000 cm$^{-1}$) intermediates were observed as the potential at was increased from 1.2 V to 2.0 V *vs.* RHE (Figs. 5e and f). The direct observation of these species provides strong support for the AEM pathway. To definitively rule out the participation of lattice oxygen, *in situ* differential electrochemical mass spectrometry (DEMS) was conducted using $^{18}O$ isotope labeling (Fig.

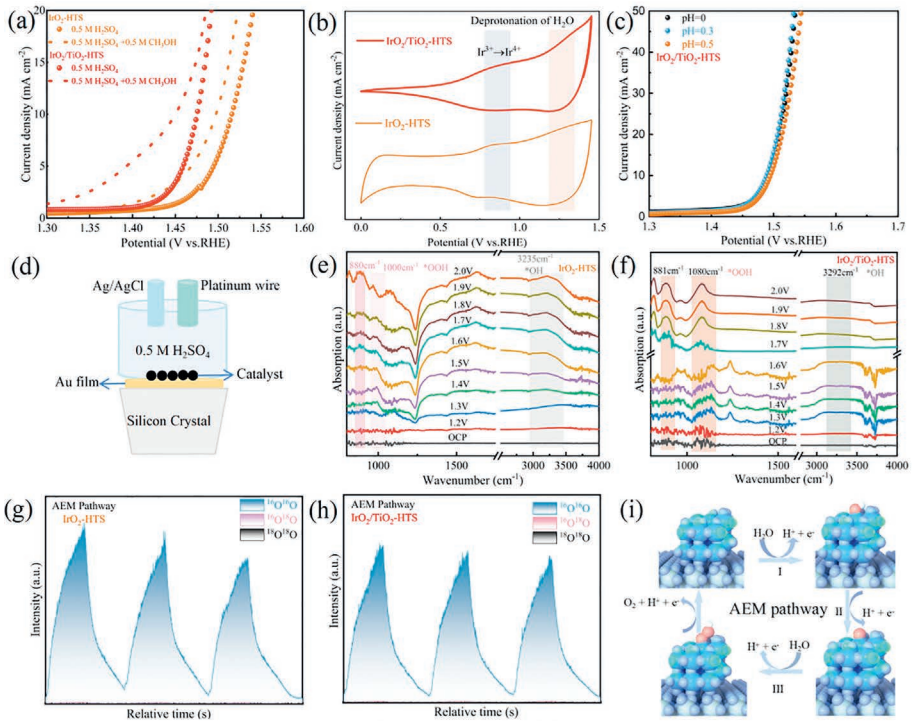



**Fig. 5.** OER mechanism analysis of $IrO_2/TiO_2$-HTS. (a) LSV curve of $IrO_2/TiO_2$-HTS and $IrO_2$-HTS catalysts in 0.5 mol/L $H_2SO_4$ electrolyte with/without 0.5 mol/L $CH_3OH$. (b) Cyclic voltammetry (CV) curve of $IrO_2/TiO_2$-HTS and $IrO_2$-HTS catalysts in 0.5 mol/L $H_2SO_4$ electrolyte at scan rate of 50 mV/s within 1-1.4 V *vs.* RHE. (c) pH dependence on the LSV curve for $IrO_2/TiO_2$-HTS in $H_2SO_4$ electrolyte. (d) *In situ* ATR-SEIRAS schematic diagram. (e) *In situ* ATR-SEIRAS analysis of the $IrO_2$-HTS catalysts. (f) *In situ* ATR-SEIRAS analysis of the $IrO_2/TiO_2$-HTS catalysts. (g) DEMS analysis of the $IrO_2$-HTS catalysts. (h) DEMS analysis of the $IrO_2/TiO_2$-HTS catalysts. (i) Schematic illustration of the OER mechanism for $IrO_2/TiO_2$-HTS.

S33 in Supporting information). After pre-adsorbing $^{18}O$-containing species onto the catalyst surface, the OER was carried out in an $H_2{}^{16}O$ electrolyte. For both catalysts, the evolved oxygen consisted exclusively of $^{32}O_2$ ($^{16}O$ – $^{16}O$), with no detectable $^{36}O_2$ ($^{18}O$ – $^{18}O$) signal (Figs. 5g and h). Collectively, these results confirm that the OER on the $IrO_2/TiO_2$-HTS catalyst proceeds *via* the AEM pathway, where all oxygen atoms in the evolved $O_2$ originate from water molecules rather than the catalyst lattice (Fig. 5i).

Overall, we developed a rapid, cost-effective, and scalable HTS technique for fabricating $TiO_2$-supported $IrO_2$ catalysts with abundant oxygen vacancies. The versatility was confirmed by successful extension to binary system, such as Ru-doped $IrO_2/TiO_2$. The as-prepared $IrO_2/TiO_2$-HTS catalyst exhibits outstanding electrocatalytic performance, achieving a mass activity of 1081 $A/g_{Ir}$ at 1.6 V *vs.* RHE in 0.5 mol/L $H_2SO_4$. Furthermore, the catalyst has the lowest Tafel slope and minimal charge-transfer resistance, confirming rapid electron transfer and superior electrocatalytic kinetics. Chronopotentiometric tests at 10 $mA/cm^2$ showed that $IrO_2/TiO_2$-HTS remained stable for 1165 h with a voltage decay of 40 μV/h. The post-reaction characterizations confirmed minimal noble metal leaching, indicating better stability than reference catalysts. This study establishes an effective route for ultrafast synthesis of high-performance supported catalysts and advanced their potential for practical application in proton exchange membrane water electrolysis.

## Declaration of competing interest

The authors declare that they have no known competing financial interests or personal relationships that could have appeared to influence the work reported in this paper.

## CRediT authorship contribution statement

**Lingchang Kong:** Resources, Investigation. **Xiaoya Cui:** Supervision, Funding acquisition. **Yujing Li:** Project administration, Data curation. **Kaiwen Yang:** Resources, Investigation. **Hengxing Peng:** Visualization, Software. **Libing Liao:** Investigation, Formal analysis. **Guocheng Lv:** Resources, Conceptualization.

## Acknowledgments

This work was supported by the National Natural Science Foundation of China (Nos. 22479011 and 12205165), High-performance Computing Platform of China University of Geosciences Beijing, and 2025 Graduate Innovation Found Project of China University of Geosciences, Beijing.

## Supplementary materials

Supplementary material associated with this article can be found, in the online version, at doi:10.1016/j.cclet.2026.112375.

## References

[1] Y. Du, J. Liu, J. Chen, et al., Adv. Energy Mater. 15 (2025) 2404113.
[2] H. Li, S. Yuan, J. You, et al., Nano-Micro Lett. 17 (2025) 225.
[3] H. Liu, Q. Zhou, J. Yu, et al., ACS Catal. 15 (2025) 8511–8521.
[4] Y. Li, J. Zou, L. Sun, et al., Adv. Funct. Mater. 35 (2025) 2509899.
[5] K. Sun, X. Liang, X. Wang, et al., Angew. Chem. Int. Ed. 64 (2025) e202504531.
[6] Y. Song, H. Chen, X. Wang, et al., Energy Environ. Sci. 18 (2025) 130–154.
[7] J. Ge, X. Wang, H. Tian, et al., Chin. Chem. Lett. 36 (2025) 109906.
[8] H. Chen, M. Na, X. Zou, CCS Chem. 7 (2025) 3259–3274.
[9] S. Zaman, M. Khalid, S. Shahgaldi, ACS Energy Lett. 9 (2024) 2922–2935.
[10] W. Feng, B. Chang, Y. Ren, Adv. Mater. 37 (2025) 2416012.
[11] E. Cazzulani, C. Roiron, L. Zhang, et al., Adv. Sci. 12 (2025) e08036.
[12] W. Shi, T. Shen, C. Xing, et al., Science. 387 (2025) 791–796.
[13] Y. Wang, Z. Zhao, X. Liang, et al., Adv. Mater. 36 (2024) 2407717.
[14] Y. Shi, Z. Lu, L. Guo, et al., Int. J. Hydrogen Energy 43 (2018) 9133–9143.

[15] M. Kost, M. Kornherr, P. Zehetmaier, et al., ECS Meet. Abstr. (2024) 4899 MA2024-02.
[16] H. Li, Y. Xu, N. Lv, et al., ACS Sustain. Chem. Eng. 11 (2023) 1121–1132.
[17] S. Abbou, R. Chattot, V. Martin, et al., ACS Catal. 10 (2020) 7283–7294.
[18] H. Li, Y. Pan, L. Wu, et al., Int. J. Hydrogen Energy. 48 (2023) 26021–26031.
[19] Y. Wang, M. Zhang, Z. Kang, et al., Nat. Commun. 14 (2023) 5119.
[20] Y. Zeng, L. Yan, S. Tian, et al., ACS Appl. Mater. Interfaces 15 (2023) 47103–47110.
[21] G. Li, A. Priyadarsini, Z. Xie, et al., J. Am. Chem. Soc. 147 (2025) 7008–7016.
[22] Z. Shi, J. Li, J. Jiang, et al., Angew. Chem. Int. Ed. 61 (2022) e202212341.
[23] D. Leybo, U.J. Etim, M. Monai, et al., Chem. Soc. Rev. 53 (2024) 10450–10490.
[24] L. Liu, A. Corma, Chem. Rev. 118 (2018) 4981–5079.
[25] X. Wang, Z. Qin, J. Qian, ACS Catal. 13 (2023) 10672–10682.
[26] Y. Qin, Y. Wang, R. Wen, ACS Catal. 14 (2024) 13915–13926.
[27] D. Yang, C. Zhang, Y. Qin, Nat. Commun. 16 (2025) 7236.
[28] N. Dimitrova, A. Banti, O.N. Spyridou, J. Electroanal. Chem. 900 (2021) 115720.
[29] Q. Chu, Y. Niu, H. Tao, ACS Catal. 15 (2025) 1942–1951.
[30] P. Fang, Y. Wang, F. Zhang, Adv. Funct. Mater. 35 (2025) 2501142.
[31] G. Yu, R. Li, Y. Hu, Nano Res. 17 (2024) 6903–6909.
[32] Y. Qin, Y. Huang, Q. Ye, et al., Adv. Energy Mater. 15 (2025) 2405636.
[33] Y. Liu, X. Tian, Y.C. Han, et al., Chin. J. Catal. 48 (2023) 66–89.
[34] X. Cui, Z. Zhang, Y. Gong, et al., CCS Chem. 2 (2020) 24–30.
[35] X. Cui, W. Li, Y. Liu, J. Mater. Sci. Technol. 191 (2024) 1–7.
[36] X. Hou, X. Yu, M. Liu, et al., Chin. Chem. Lett. 36 (2025) 109845.
[37] L. Li, Y. Liu, P. Kang, et al., Chin. Chem. Lett. 37 (2026) 112022.
[38] X. Cui, Y. Liu, Q. Li, et al., Chin. Chem. Lett. 36 (2025) 110069.
[39] W. Zhu, M. Ma, D. Gao, et al., Angew. Chem. Int. Ed. 64 (2025) e202423353.
[40] J. Yang, K. An, Z. Yu, et al., ACS Catal. 14 (2024) 17739–17747.
[41] X. He, J. Tan, B. Deng, et al., Adv. Funct. Mater. 35 (2025) 2416385.
[42] C. Gao, Y. Wang, S. Zhen, et al., J. Phys. Chem. C 129 (2025) 12796–12803.
[43] S. Liu, Z. Hu, Y. Wu, et al., Adv. Mater. 32 (2020) 2006034.
[44] X. Cui, Y. Liu, X. Wang, et al., ACS Nano 18 (2024) 2948–2957.
[45] X. Shan, Y. Pan, F. Cai, et al., Nano Lett. 24 (2024) 11632–11640.
[46] Z. Fang, Z. Tang, S. Lin, et al., CrystEngComm 26 (2024) 475–483.
[47] C.V. Pham, M. Bühler, J. Knöppel, M. Bierling, et al., Appl. Catal. B: Environ. 269 (2020) 118762.
[48] H.P. Tran, H.N. Nong, M. Zlatar, et al., J. Am. Chem. Soc. 146 (2024) 31444–31455.
[49] R. Jiang, Y. Da, X. Han, et al., Cell Rep. Phys. Sci. 2 (2021) 100302.
[50] Z. Zheng, C. Zhang, J. Li, et al., J. Hazard. Mater. 474 (2024) 134710.
[51] P. Fang, Y. Wang, F. Zhang, et al., Adv. Funct. Mater. 35 (2025) 2501142.
[52] L. Ai, Y. Tian, T. Xiao, et al., Fuel. 373 (2024) 132368.
[53] J. Sui, H. Sun, F. Wang, et al., Small. 21 (2025) 2505131.
[54] Z. Ma, S. Zhan, Y. Zhang, et al., Adv. Mater. 37 (2025) 2416581.
[55] X. Cheng, Y. Liu, W. Zhong, et al., Adv. Sci. 12 (2025) e09293.
[56] Y. Wang, Y. Qin, R. Wen, et al., Small 20 (2024) 2401964.
[57] Q. Cheng, Y.J. Yuan, R. Tang, et al., ACS Catal. 12 (2022) 2118–2125.
[58] C. Yang, Y. Zhu, F. Zhang, et al., Adv. Mater. 37 (2025) 2507560.
[59] L. Wang, L. Shi, Q. Liu, et al., ACS Catal. 13 (2023) 7322–7330.
[60] H. Zhang, F. Yi, M. Xu, et al., Int. J. Hydrogen Energy 168 (2025) 151059.
[61] X. Teng, K. Zhang, Z. Yang, et al., Electrochim. Acta 549 (2026) 148065.
[62] C. Wang, X. Wu, H. Sun, et al., Energy Environ. Sci. 18 (2025) 4276–4287.
[63] J. Dai, Z. Shen, Y. Chen, et al., J. Am. Chem. Soc. 146 (2024) 33663–33674.
[64] X. Chen, H. Ma, X. Wang, et al., J. Am. Chem. Soc. 147 (2025) 20600–20611.
[65] Y. Qin, X. Niu, R. Zhao, et al., ACS Catal. 14 (2024) 12970–12981.
[66] L. Xu, L. Lu, N. Xu, et al., Angew. Chem. Int. Ed. 64 (2025) e202510965.
[67] L. Wang, S.F. Hung, S. Zhao, et al., Nat. Commun. 16 (2025) 3502.